Aqueous structure of lanthanide-EDTA coordination complexes determined by a combined DFT/EXAFS approach

Adam Smerigan[a], Sayani Biswas[b], Fernando D. Vila[c], Jiyun Hong[d], Jorge Perez-Aguilar[d], Adam S. Hoffman[d], Lauren Greenlee[a], Rachel B. Getman[b], Simon R. Bare[d]**

[a] Department of Chemical Engineering, The Pennsylvania State University, University Park, PA 16802, USA

[b] Department of Chemical and Biomolecular Engineering, Clemson University, Clemson, SC 29634, USA

[c] Department of Physics, The University of Washington, Seattle, WA 98195, USA

[d] SSRL, SLAC National Accelerator Laboratory, Menlo Park, CA 94025, USA

*rgetman@clemson.edu

*simon.bare@slac.stanford.edu

KEYWORDS: Density functional theory (DFT), Extended X-ray Absorption Fine Structure (EXAFS), Lanthanide (Ln), Rare Earth Elements (REE), Ethylenediaminetetraacetic acid (EDTA), Coordination Complex, Coordination Structure

Abstract

Sustainable production of rare earth elements (REEs) is critical for technologies needed for climate change mitigation, including wind turbines and electric vehicles. However, separation technologies currently used in REE production have large environmental footprints, necessitating more sustainable strategies. Aqueous, affinity-based separations are examples of such strategies. To make these technologies feasible, it is imperative to connect aqueous ligand structure to ligand selectivity for individual REEs. As a step toward this goal, we analyzed the extended x-ray absorption fine structure (EXAFS) of four lanthanides (La, Ce, Pr, and Nd) complexed by a common REE chelator, ethylenediaminetetraacetic acid, or EDTA, to determine the aqueous-phase structure. Reference structures from density functional theory (DFT) were used to help fit the EXAFS spectra. We found that all four Ln-EDTA coordination complexes formed 9-coordinate structures with 6 coordinating atoms from EDTA (4 carboxyl oxygen atoms and 2 nitrogen atoms) and 3 oxygen atoms from water molecules. All EXAFS fits were high quality (R-factor < 0.02) and showed decreasing average first-shell coordination distance across the series (2.62-2.57 Å from La-Nd), in agreement with DFT (2.65-2.56 Å from La-Nd). The insights determined herein will be useful in the development of ligands for sustainable REE separation technologies.

Introduction

The Intergovernmental Panel on Climate Change predicts that an increase in Earth's temperature of 1.5°C above pre-industrial levels would lead to a decrease in the standard of living globally.[1] Rare earth elements (REEs), consisting of the lanthanides (Ln), yttrium, and scandium, are essential for many technologies being considered to limit global warming, such as wind turbines (magnets), electric vehicles and energy storage (batteries), emissions control (catalysts), energy efficiency (LEDs), and more.[2] However, the current method used to produce REEs, liquid-liquid extraction (LLE), has a large environmental footprint.[3–6] LLE uses organic solvents mixed with extractants to selectively separate lanthanides by preferentially transferring REEs from an aqueous leachate into the organic phase.[7] This separation can take up to three hundred solvent extraction stages to achieve a pure product.[8] Since most REE pre-concentration is performed in the aqueous phase, aqueous separation methods are a convenient alternative for reducing the environmental impact of REE production.[9]

Various aqueous separation technologies exist for the recovery of REEs, the most developed being ion exchange.[10] Ion exchange can obtain high purity individual lanthanides (99.99%) but has high costs and creates large amounts of secondary waste, limiting its application.[11] Consequently, new technologies that are lower cost and produce less waste, such as adsorption and other affinity-based separations, must be developed.[12,13] Developing affinity-based technologies requires ligands (or other organic extractants) that have strong binding and selectivity for individual lanthanides.[14] Specifically, more selective ligands must be designed by making structures that utilize steric strain and outer-sphere coordination to achieve an efficient separation.[15–18] Therefore, an understanding of how ligand coordination geometry affects binding and selectivity is integral in further developing these technologies.[13,19,20] Historically, much of this work for the f-block elements has been done for the actinide series.[21–24] Considering the wide

variety of applications for lanthanides in modern technologies, there is a need to understand the structure of lanthanide complexes in water and create design rules for making aqueous ligands that bind strongly and selectively for individual REEs.

Ethylenediaminetetraacetic acid (EDTA), a common transition metal chelator utilized in REE ion exchange[25–27], has been the subject of many structural studies.[28–39] Studies generally agree that light lanthanides (lanthanides with lower atomic number) are 9-coordinate when binding with EDTA (6 sites taken by EDTA and 3 by water) before losing a water and becoming 8-coordinate for the heaviest lanthanides.[28,32,39] However, the organization of molecules and the distance of coordinating atoms to the lanthanide ion in solution remains unclear. Molecular simulations using molecular dynamics (MD) and density functional theory (DFT) have modeled the coordination structures of Ln-EDTA complexes.[28,39] The MD simulation of a La-EDTA resulted in an average La-EDTA distance considerably shorter than the distance of an AIMD simulation (2.53 ± 0.06 Å and 2.63 Å, respectively) indicating a need for structural confirmation from experimental data. To determine the structure experimentally, single crystal x-ray diffraction (SC-XRD) has been used for precipitated Ln-EDTA complexes.[30,31,33,34,36–38] XRD structures show a steady trend towards shorter first shell bond distances across the Ln series (2.62 Å and 2.54 Å for La and Nd, respectively). However, the solid crystals studied may not represent the actual structure of the complex in solution due to changes in geometry during crystallization (i.e., crystal packing forces).[40] One technique that directly probes the local structure of the Ln atoms in solution is x-ray absorption spectroscopy (XAS). The extended x-ray absorption fine structure (EXAFS) region of XAS spectra measures the photoelectron backscattering of neighboring atoms to the absorbing atom. This backscattering makes the EXAFS sensitive to the distance and element of neighboring scattering atoms since each scatterer will contribute to the phase and amplitude of the signal. To

determine the structure, theoretical scattering contributions from reference structures are fit to the EXAFS spectra. EXAFS studies of La-EDTA and Nd-EDTA have determined first shell distances (2.48 Å and 2.48 ± 0.09 Å, respectively) but acknowledged challenges in the modelling that lead to smaller than expected distances.[28,41] These studies and other conventional EXAFS studies have used reference structures derived from XRD to model the EXAFS. However, these references do not directly relate to the structure in solution and therefore may result in unphysical structures.[42] Studies have begun to couple MD/DFT simulations with experimental EXAFS to overcome this issue, validate simulations, and gain additional insight into the coordination chemistry of Ln complexes in solution.[15,16,43–46]

Herein, we further address this issue by using optimized structures from DFT to model the EXAFS and determine the aqueous structure of La-, Ce-, Pr-, and Nd-EDTA complexes. Using these DFT optimized structures, we achieve quality EXAFS fits for each Ln-EDTA complex in solution. We find that all four Ln complexes are coordinated by 3 oxygen atoms from water, 4 oxygen atoms from EDTA, and 2 nitrogen atoms from EDTA. We determine the bonding distances of these inner sphere coordinating atoms to the Ln atom and compare them to results from other solution-phase and solid-phase studies. The determination of coordination structures, such as for these Ln-EDTA complexes, is an important first step towards designing selective ligands for aqueous REE separations.

Materials and Methods

DFT Calculations

DFT calculations are performed with the Gaussian 16 software using the M06-L functional. This functional is chosen because it has shown good balance between computational tractability and accuracy for systems containing lanthanides in their +3 oxidation state.[47] Geometric optimizations

of the aqueous Ln-EDTA complex models are performed at 0 K using the Def2-SVP basis set for H, C, O and N atoms of EDTA and water molecules[48] and Def2-TZVPP with associated effective core potentials (ECPs) for the lanthanide cations La^{3+}, Ce^{3+}, Pr^{3+} and Nd^{3+}.[49–51] Test calculations show that choice of basis set and DFT functional results in a maximum of 0.3 Å difference in the interatomic distances of the lanthanide ions and their coordinating atoms (Figures S1 and S2).

EDTA is known to form stable metal complexes in its completely deprotonated form.[52] EDTA is hence modelled to be completely deprotonated with a –4 charge and each lanthanide cation is modelled with a +3 charge. This results in an overall charge of –1 on each Ln-EDTA complex. Multiple possible multiplicities are considered for the isolated lanthanide cations (Tables S2 and S3). Specifically, multiplicities of 1, 3, 5 and 7 are considered for La^{3+} and Pr^{3+} while multiplicities 2, 4, 6 and 8 are considered for Ce^{3+} and Nd^{3+}. The structures for each aqueous Ln-EDTA complex are calculated at the multiplicity that yields the lowest electronic energy for each isolated lanthanide cation (1 for La^{3+}, 2 for Ce^{3+}, 3 for $Pr^{3+}$and 4 for Nd^{3+}). The initial structure of the Ln-EDTA complex is modelled such that the lanthanide cation is chelated by the six potential bonding sites of the EDTA, four carboxyl and two amino groups, similar to hexadentate complexes that EDTA forms with other metals in their +3 oxidation state (Figure 1).[53] During geometric optimization of the Ln-EDTA complex, all atoms are allowed to relax. Once an optimized geometry is obtained, explicit water molecules are added to the system one at a time and all the atoms are allowed to relax again. This is done for up to seven explicit water molecules to obtain the complete structure of the first coordination shell around each Ln cation. These Ln-EDTA complex structures with explicit water molecules are then modelled and optimized under implicit water solvent using the Polarizable Continuum Model (PCM) method (Figure S3). Vibrational frequencies are calculated for all the optimized structures. Example Gaussian input

files for geometry optimizations and vibrational frequency calculations are provided in the Supporting Information. The theoretical MSRDs are calculated with the DMDW code,[54] using the DFT Hessian from the computed vibrational frequencies. Given the complexity of the vibrational density of states of these systems, a total of 40 Lanczos poles are needed to obtain MSRDs converged to $0.01*10^{-3}$ $Å^2$. All MSRDs are calculated at 300 K. The total theoretical MSRDs for each EXAFS fitted shell is obtained by adding the static MSRD to the average of the thermal MSRDs.

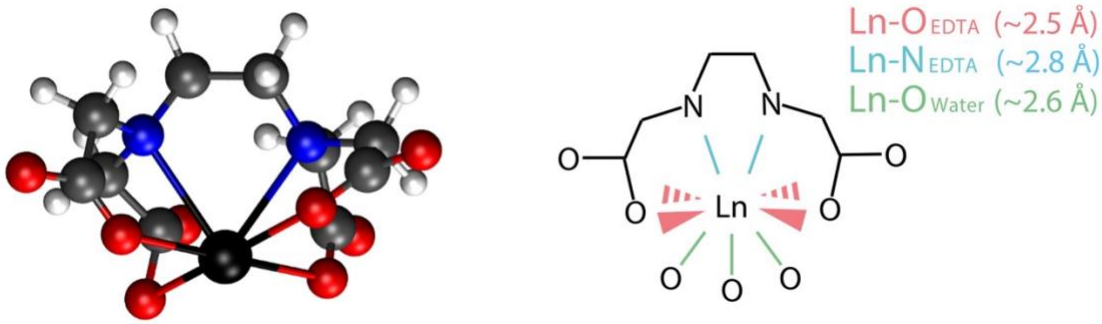

Figure 1: Initial input structure of the La-EDTA complex for geometric optimization (color key: carbon = gray, oxygen = red, hydrogen = white, nitrogen = light blue, and lanthanum = black) (left image). A simplified Ln-EDTA structure showing the first shell coordination bonds colored by atom and molecule (right image). Only one symmetrical half of the EDTA molecule is shown for clarity. Stereochemical bonds show the four coordinating EDTA oxygen atoms.

Sample Preparation for X-ray Absorption Spectroscopy

The lanthanide chloride was purchased from Sigma Aldrich at ≥99.9% trace metal purity. The EDTA was purchased from Sigma Aldrich at ≥99% purity. The lanthanide chlorides were kept with desiccant to prevent moisture from entering the compound prior to sample preparation. Stock solutions of lanthanide chloride and EDTA were made in MilliQ water (28 MΩ·cm). The pH of each stock solution was adjusted to 6 using NaOH from Sigma Aldrich at ≥99.9% purity. Samples consisted of 0.05 M lanthanide chloride and 0.05 M EDTA and were sealed inside polyethylene

x-ray fluorescence cups (SPEX™ SamplePrep 3577) using a 3.6 µm Polyester (mylar) film window from Somar International.

X-ray Absorption Spectroscopy

The x-ray absorption spectra were collected at beamline 9-3 at the Stanford Synchrotron Radiation Lightsource within the SLAC National Accelerator Laboratory. Beamline 9-3 is a wiggler-based side station equipped with a Si(220), φ=90°, double bounce liquid nitrogen-cooled monochromator and Rh-coated collimating and focusing mirrors located before and after the monochromator, respectively. The beamline 9-3 mirrors were operated in a 10 KeV cutoff mode with the monochromator detuned 40% to minimize the effect of harmonics and beam size was 1.0 mm vertical and 4.0 mm horizontal. The flux of the X-ray is estimated to be $2x10^{12}$ photons per second in a spot size of 1x4 mm^2. EXAFS spectra were collected in step-scanning mode with the samples in a fluorescence geometry (sample at a 45° angle to the incident beam) using a PIPS diode with 10 cm Soller Slits to minimize signal from the scattered beam. Reference spectra of a manganese foil (calibrated to 6539.0 eV) was collected simultaneously as an internal energy standard by an off-axis photodiode. The Mn foil was additionally scanned without the sample to be used for energy alignment in the data processing. 2-4 spectra of each sample were collected to achieve sufficient signal-to-noise.

EXAFS Analysis

Raw XAS data was processed in Athena from the Demeter software package.[55] Using the first derivative maxima to define the edge position, the Mn reference foil was calibrated to its tabulated edge energy, 6539.0 eV.[56] The Mn reference spectrum collected during each Ln scan was aligned to the foil spectrum to calibrate the sample data and determine the edge energy of the lanthanide. Athena was used for energy calibration, normalization of spectra for XANES comparison, and EXAFS extraction.

To collect EXAFS data for the lanthanides, the use of the high energy k-edges induces experimental complications and is often precluded by the need for high energy beamlines that are not present at many synchrotrons. In contrast, the lower energy L-edges of the lanthanides are accessible and have been used in many studies looking at the coordination structure of Ln in solution.[15,17] Despite this advantage, the L-edge EXAFS of the lanthanides poses a few challenges for EXAFS modelling. Light lanthanides (low atomic number) have strong multielectron excitations (MEEs) that have been shown to cause errors of 0.02 Å in interatomic distance[57,58] and 10% in CN during fitting.[59,60] Multielectron excitations (MEE) were removed from all spectra using the removal tool in Athena. The EXAFS data before and after MEE removal are available in Figures S4-S7. The EXAFS of the L-edges of the lanthanides naturally have limited k-range due to the presence of the next absorption edge. For instance, the EXAFS of the L_3 edge of lanthanum (5483 eV) is interrupted by the L_2 edge (5891 eV) which leaves 408 eV (~10.3 $Å^{-1}$) available for analysis. Though the available *k*-range increases across the lanthanide series, a strong post-edge feature begins to influence the early EXAFS (<3.3 Å) of praseodymium and neodymium making it unusable. A spline was applied starting from 2.4 $Å^{-1}$ to attempt to reduce the influence of this feature and use more of the *k*-range, however, the fit was still poor. Therefore, a limited *k*-range was used. This limited *k*-range causes the peaks in the resulting Fourier transform (FT) to be poorly resolved.[61] Despite the challenges that limited k-range and MEEs impose on the EXAFS analysis, use of the L-edges of the lanthanides is still more feasible than the k-edges. Further, the smaller core-hole lifetime broadening of the L-edges has been useful for observing high frequency signals important for outer sphere coordination and geometry determination making the L-edges ideal for use in this study.[44,62]

Artemis from the Demeter package[55] was used to model the EXAFS spectra. A structure file input was created using the coordinates of atoms from DFT for the generation of theoretical scattering paths. FEFF input files for each coordination complex are available in the SI. Nearly degenerate scattering paths were condensed to a single path with a 'fuzziness margin' of 0.15 Å. This functionality is useful for greatly reducing the complexity and the information content used in the EXAFS modelling. However, applying fuzzy degeneracy has been shown to modify the signal due to the change in static disorder[63] and can contribute as much as $23*10^{-3}$ $Å^2$ to MSRD values. The MSRD values obtained here were confirmed to be within error of values observed in other studies of Ln complexation in solution.[15,44] The amplitude reduction factor (S_o^2) was set to 1.0 while fitting all samples (no reduction applied), as done in other studies.[35,44,60,64] The degeneracy (N) of each scattering path was set at the value designated by the FEFF output. The difference in edge energy (ΔE_o) between the experiment and the FEFF calculation was varied during the fitting process. All scattering paths shared the same value of ΔE_o since all the scattering paths came from the same FEFF calculation. The change in path length from the input structure (ΔR) and the mean square radial displacement, MSRD (σ^2), were varied parameters in the fit. Due to the limited information content of these EXAFS data, some guess parameters were shared between scattering paths. Table 1 shows the parameterization strategy for a representative Ln-EDTA complex. Parameters were constrained to paths based on the anticipated behavior of the structure. For instance, the disorder of a scattering path is related to the σ^2 of the path. The disorder of the EDTA molecule was expected to be less than that of coordinated waters, so a different σ^2 was given to the first shell water oxygens than the first shell EDTA oxygens. A new σ^2 was given for all second shell scatterers. The multiple scattering path was constrained by doubling the σ^2 of the first shell EDTA oxygen atoms. All σ^2 values were constrained to be positive. Different ΔR

were given to first shell EDTA and water atoms. Second shell carbon and oxygen scatterers were given a new ΔR. The following fitting ranges were used for each Ln-EDTA complex: La-EDTA with a *k*-range: 2.5-8.6 $Å^{-1}$ and *R*-range: 1.5-4.8 Å, Ce-EDTA with a *k*-range: 2.5-9.4 $Å^{-1}$ and *R*-range: 1.5-5.3 Å, Pr-EDTA with a *k*-range: 3.3-9.0 $Å^{-1}$ and *R*-range: 1.5-5.2 Å, Nd-EDTA with a *k*-range: 3.1-9.0 $Å^{-1}$ and *R*-range: 1.3-5.1 Å).

Table 1: EXAFS fitting parameters for the paths generated from the structures shown in Figure 2. The first shell coordinated oxygens are subscripted by the molecule they belong to (EDTA and water).

Scattering Path	Approximate Path Length (Å)	MSRD (σ^2)*	Deviation in Path Length (ΔR)*	Edge Energy (ΔE_o)*
Ln-O_{EDTA}	2.5	a	a	a
Ln-O_{water}	2.6	b	b	a
Ln-N	2.8	a	a	a
Ln-C	3.3	c	c	a
Ln-C	3.4	c	c	a
Ln-C	3.5	c	c	a
Ln-O	4.3	c	d	a
Ln-O	4.5	c	d	a
Ln-C-O	4.7	a†	c	a

S_o^2 was set to 1.0 for each path and was not varied in the fit. Values of N were set at the value designated by the FEFF output for each path.

*Scattering paths sharing the same letter for a parameter are constrained to the same value.

†Value of parameter is twice the fitted parameter value.

Results

The EXAFS best fit models using DFT optimized structures of La, Ce, Pr, and Nd coordinated by EDTA are shown in Figure 2 (fits in k-space are shown in Figures S8-11). The magnitude and real part of the FT of each Ln L-edge EXAFS spectrum and the best fit model are shown for each

coordination complex. In each complex, the lanthanide ion is 9-coordinate, as shown in Figure 1 (right). EDTA coordinates the lanthanide ion with four oxygen atoms and two nitrogen atoms, while water molecules coordinate the remaining 3 oxygen atoms to fill the first coordination sphere. The other water molecules shown in Figure 2 form part of a second coordination sphere around 4-4.5 Å from the Ln atom and were essential to fitting the EXAFS further in R-space. The magnitude of the FT of the EXAFS has a large peak at ~2 Å that is primarily due to first shell oxygen and nitrogen scatterers. Several shoulders are observed with diminishing magnitude as they progress further in R-space as a result of scattering from the second shell carbon and oxygen atoms.

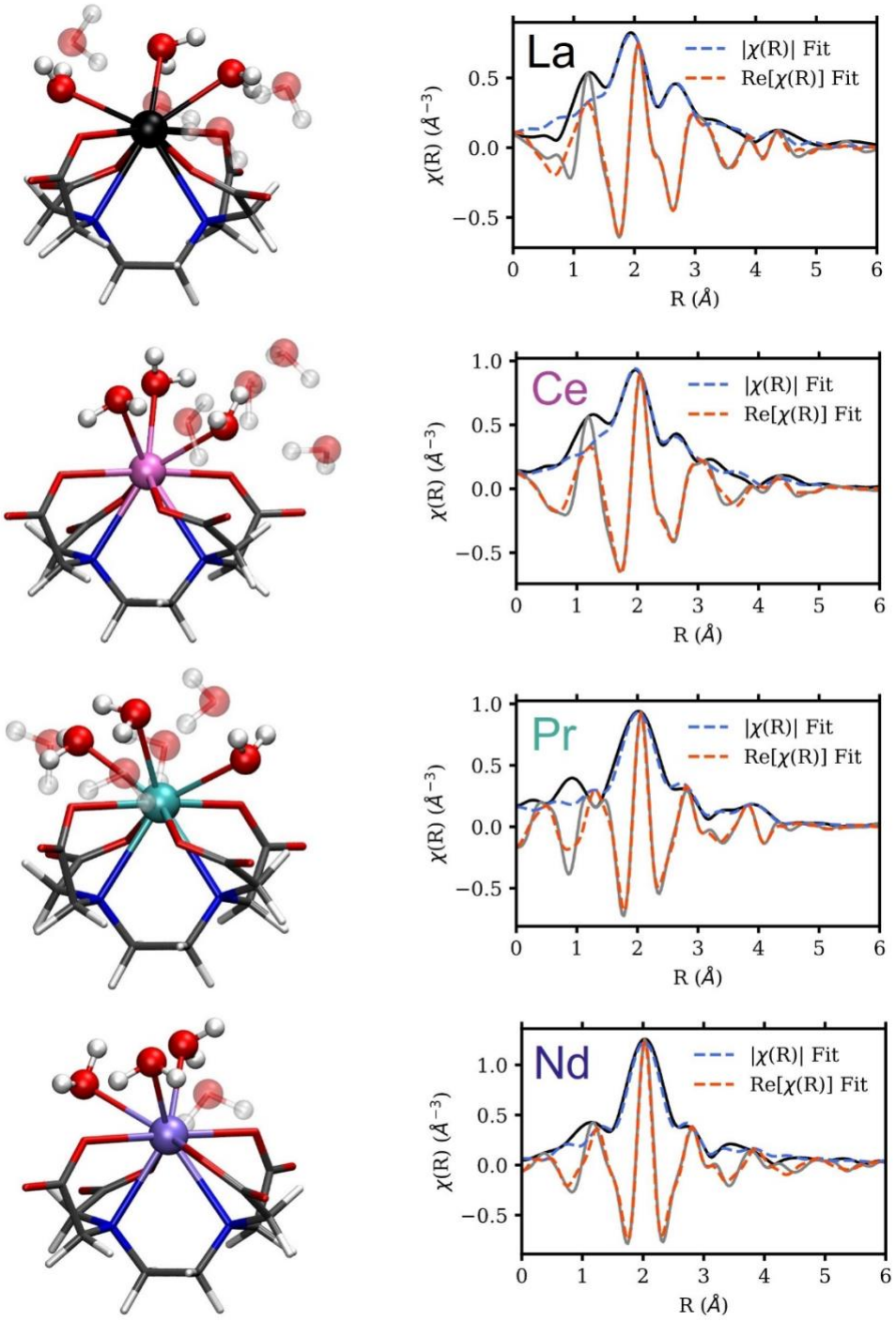

Figure 2: The Ln-EDTA DFT optimized structures using a stick model to show the EDTA molecule and a ball and stick model to show coordinated water molecules where outer sphere water molecules appear transparent (element color key: red=O, blue=N, gray=C, white=H, black=La, pink=Ce, teal=Pr, purple=Nd) (left) and the magnitude and real part of the FT for each Ln L-edge EXAFS spectrum (solid lines) with the best fit EXAFS model (dotted lines) (right). Fitting ranges for each Ln-EDTA complex are (La-EDTA: *k*-range: 2.5-8.6 $Å^{-1}$ and *R*-range: 1.5-4.8 Å, Ce-

EDTA: *k*-range: 2.5-9.4 $Å^{-1}$ and *R*-range: 1.5-5.3 Å, Pr-EDTA: *k*-range: 3.3-9.0 $Å^{-1}$ and *R*-range: 1.5-5.2 Å, Nd-EDTA: *k*-range: 3.1-9.0 $Å^{-1}$ and *R*-range: 1.3-5.1 Å).

The best-fit EXAFS models make good chemical sense for scattering paths where the absorber and backscattering atoms are at a bonding or a near-neighbor distance. Paths in the second shell (~4-4.5 Å) have fitted parameters that are sometimes outside the conventional ranges. For example, the best fit models shifted the second shell Ln-O scattering paths ~0.2 Å longer (e.g., the longest second shell Ln-O path increases from 4.51 Å in DFT to 4.75 Å in the EXAFS model in Table 2). We attribute these larger shifts to limitations in the model systems. Since DFT calculations cannot incorporate a full water structure, the number of water molecules used in our models was limited (to 7 for Ln^{3+}, Ce^{3+}, and Pr^{3+} and 4 for Nd^{3+}; see Figure 2). Hence, the distance of the simulated second shell waters is shifted to longer distances to compensate for the absence of additional explicit water molecules, which would exist in the experimental system and lead to backscattering. To capture this backscattering computationally, multiple configurations of the second solvation shell would be needed, since the second solvation shell is significantly disordered. Doing this would require multiscale modeling and could be an area of future work.

Table 2 shows the results from the best fit of the EXAFS for each lanthanide complex. Each of the Ln-EDTA structures had similar single-scattering paths that contributed meaningfully to the spectra: one inner-sphere oxygen scattering path from EDTA (O_{EDTA}), one oxygen path from inner sphere water (O_{water}), one inner-sphere nitrogen path from EDTA, two or three outer-sphere carbon paths from EDTA, and two or three outer-sphere oxygen paths from EDTA and water. The Ce-EDTA structure had one significant multiple-scattering path between an EDTA oxygen and carbon that was included as well. Using these paths and the constraints from Table 1, good fits were achieved for each lanthanide (R-factors < 0.02).

Table 2: EXAFS fitting results for the structures shown in Figure 2. The first shell coordinated oxygens are subscripted by the molecule they belong to (EDTA and water).

Complex	Scattering Path	N	σ^2 (10^{-3} Å^2)	$\sigma^2_{tot, DFT}$ (10^{-3} Å^2)	R (Å)	R_{DFT} (Å)	ΔE_o (eV) k-range (Å^{-1}) R-range (Å) R-factor Reduced χ^2
La-EDTA	La-O_{EDTA}	4.0	7.0 ± 2.3	9.0	2.53 ± 0.01	2.53[a]	6.33 ± 2.28
	La-O_{water}	3.0	22. ± 7.5	12.5	2.59 ± 0.04	2.69[a]	2.5-8.6
	La-N	2.0	7.0 ± 2.3	10.2	2.84 ± 0.01	2.83[a]	1.5-4.8
	La-C	5.0	3.4 ± 3.0	8.4	3.39 ± 0.04	3.38[a]	0.009
	La-C	3.0	3.4 ± 3.0	11.4	3.52 ± 0.04	3.54[a]	133
	La-C	2.0	3.4 ± 3.0	9.0	3.64 ± 0.04	3.65[a]	
	La-O	1.0	3.4 ± 3.0	21.6	4.28 ± 0.02	4.04[a]	
	La-O	5.0	3.4 ± 3.0	16.1	4.75 ± 0.02	4.51[a]	
Ce-EDTA	Ce-O_{EDTA}	4.0	7.6 ± 2.3	8.6	2.48 ± 0.03	2.47 [a]	7.48 ± 0.944
	Ce-O_{water}	3.0	7.7 ± 4.0	12.5	2.59 ± 0.03	2.65 [a]	2.5-9.4
	Ce-N	2.0	7.6 ± 2.3	8.6	2.80 ± 0.03	2.78 [a]	1.5-5.3
	Ce-C	3.0	9.4 ± 3.5	10.4	3.32 ± 0.03	3.32 [a]	0.015
	Ce-C	5.0	9.4 ± 3.5	10.3	3.46 ± 0.03	3.47 [a]	413
	Ce-C	2.0	9.4 ± 3.5	9.0	3.57 ± 0.03	3.58 [a]	
	Ce-O	3.0	9.4 ± 3.5	22.0	4.42 ± 0.06	4.23 [a]	
	Ce-O	3.0	9.4 ± 3.5	11.8	4.75 ± 0.06	4.55 [a]	
	Ce-O-C	4.0	15. ± 5.2		4.60 ± 0.06	4.61 [a]	
Pr-EDTA	Pr-O_{EDTA}	4.0	2.2 ± 3.9	8.9	2.47 ± 0.04	2.44 [a]	7.02 ± 2.61
	Pr-O_{water}	3.0	0.0 ± 4.8	12.2	2.60 ± 0.04	2.66 [a]	3.3-9.0
	Pr-N	2.0	2.2 ± 3.9	10.4	2.80 ± 0.04	2.77 [a]	1.5-5.2
	Pr-C	5.0	7.0 ± 5.8	7.8	3.22 ± 0.07	3.31 [a]	0.015
	Pr-C	5.0	7.0 ± 5.8	12.9	3.44 ± 0.07	3.52 [a]	505
	Pr-O	2.0	7.0 ± 5.8	35.1	4.18 ± 0.06	3.89 [a]	
	Pr-O	5.0	7.0 ± 5.8	15.5	4.72 ± 0.06	4.43 [a]	
Nd-EDTA	Nd-O_{EDTA}	4.0	0.6 ± 3.2	8.9	2.47 ± 0.04	2.43 [a]	10.5 ± 2.09
	Nd-O_{water}	3.0	0.0 ± 4.1	10.6	2.58 ± 0.04	2.63 [a]	3.1-9.0
	Nd-N	2.0	0.6 ± 3.2	8.1	2.75 ± 0.04	2.71 [a]	1.3-5.1
	Nd-C	4.0	9.5 ± 8.0	8.4	3.27 ± 0.07	3.28 [a]	0.019
	Nd-C	6.0	9.5 ± 8.0	10.3	3.46 ± 0.07	3.47 [a]	433
	Nd-O	1.0	9.5 ± 8.0	22.3	3.70 ± 0.14	3.90 [a]	
	Nd-O	2.0	9.5 ± 8.0	13.6	4.15 ± 0.14	4.34 [a]	
	Nd-O	2.0	9.5 ± 8.0	10.1	4.35 ± 0.14	4.55 [a]	

For all paths, S_o^2 was set to 1.0. [a]Average of distances.

The Nd-O_{EDTA} scattering path was the shortest (2.43 Å) with the Ln-O_{EDTA} path length increasing as we moved to the left across the periodic table to La (2.53 Å). The Ln-O_{water} scattering path did not show a systematic change in distance (2.58-2.60 Å) as a function of Ln. However, the σ^2 of these oxygens decreased steadily from La to Nd (0.022 to 0.000 $Å^2$, respectively) indicating decreasing disorder of these water molecules. This decreasing disorder was also observed (to a lesser degree, 12.54 to 10.58 $*10^{-3}$ $Å^2$ from La to Nd) in theoretical MSRD calculated from the DFT optimized structure (Table 2). The discrepancy between these values indicates that the experimental and theoretical approaches struggle to capture a realistic conformation of these water molecules (likely due to the influence of the disordered outer sphere coordinated waters on the first shell coordinated waters (Figure S3)). Future work can explore performing EXAFS modelling on a library of potential DFT structures to identify the structures most representative of what was observed experimentally and examine water coordination more closely.

The MSRDs determined in this study are within uncertainty of literature values of other Ln-polyaminocarboxylate complexes.[65–69] The use of a large fuzziness margin to simplify the analysis may have led to more uncertainty in the absolute value of the MSRDs. However, by reducing the information content required, we were able to design a model that is simple, uses known physical aspects of the system, and is flexible/generalizable for any lanthanide ion (meeting all three criteria for a defensible model[61]). Therefore, though the absolute value of the MSRD is more uncertain, the decreasing trend of the MSRDs across the lanthanide series is significant.

In other studies, the decreasing disorder of first coordination sphere atoms across the lanthanide series has been observed as well.[39,44,70] This decreasing disorder could indicate that the inner sphere waters are more organized as we move across the lanthanide series. Indeed, DFT calculations show that inner sphere waters bind stronger to Nd than to La, Ce and Pr (Table S4 and Table S6),

supporting this suggestion. Steric effects between the ligand and water molecules and coordination geometry around the Ln atom may also play roles in the organization of these water molecules.[71]

The inner-sphere nitrogen scattering paths (e.g., bond lengths) were shortest in the Nd complex (2.75 ± 0.04 Å) and increased up to 2.84 ± 0.01 Å (La) while moving to the left across the periodic table. The carbon atoms are located slightly further from the lanthanide atom (3.22-3.64 Å) and consist of two or three significant scattering paths. Two or three second shell (3.70-4.75 Å) oxygen scattering paths were included for each lanthanide. These oxygen scattering paths had the largest deviations from the DFT structure (~0.2 Å) as discussed earlier. An EXAFS model excluding these second shell paths (a one-shell model) resulted in fits with lower statistical quality. The second shell paths are necessary for this Ln-EDTA system since EDTA (a multidentate ligand) has high order and rigidity causing the EXAFS signal from outer sphere scattering to remain significant. Additional details pertaining to the one-shell and two-shell EXAFS models are contained within the supplementary information (Figure S12 and Table S5). Other than the scattering distances of the second shell oxygen paths included in the two-shell model, scattering distances were similar (~0.1 Å or less) to the interatomic distances in the optimized DFT geometry.

The interatomic distances from the lanthanide atom to the first shell coordinating atoms as determined by EXAFS and DFT are compared in Figure 3. The difference in distances between EXAFS and DFT structures are of a similar magnitude to differences observed in other studies of lanthanide and actinide complexes with polyaminocarboxylates.[15,72] The general trends are the same and show that distances between the coordinating ligands and the lanthanide ions decrease as we move to the right across the periodic table. This trend is consistent with decreasing ionic radius across the lanthanide series (the lanthanide contraction[73]) and is observed in other studies of lanthanides bound by ligands.[15,28,44,71]

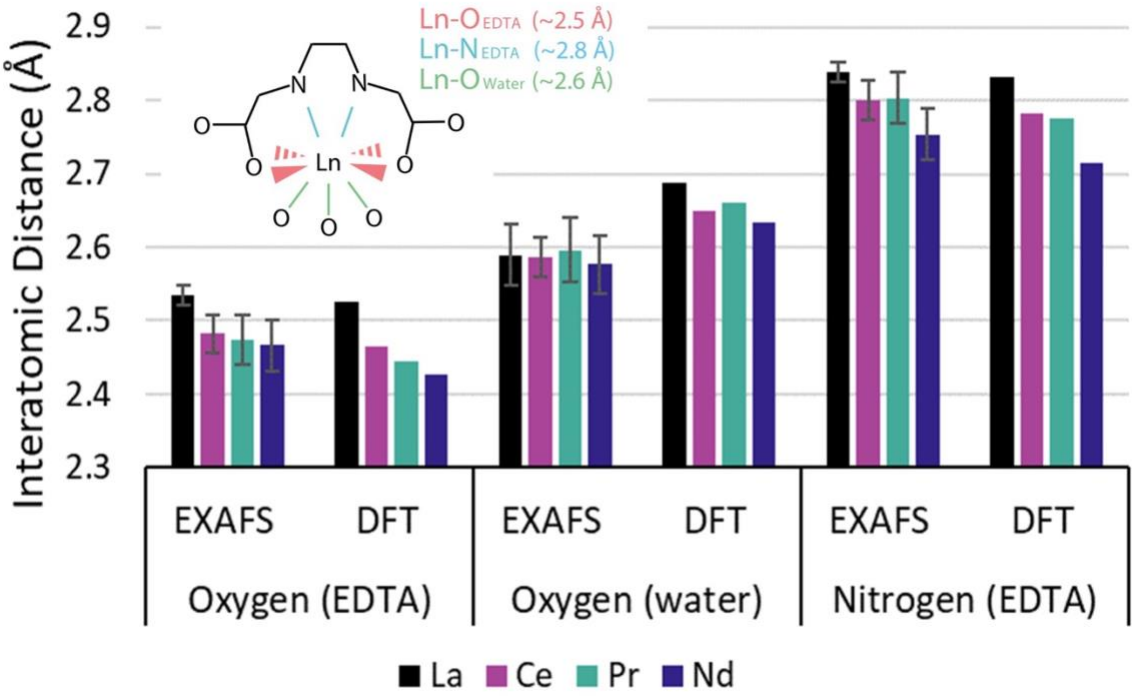

Figure 3: The average distance determined by EXAFS analysis and DFT from the lanthanide atom to its inner sphere coordinating atoms: the four EDTA oxygen atoms, the three water oxygen atoms, and the two EDTA nitrogen atoms.

Discussion

Studies examining the complexation of lanthanides by EDTA have primarily used solid phase XRD to determine coordination structure. The distances of inner sphere coordinating atoms to the lanthanides determined from XRD were compared to the EXAFS results of this study in Figure 4.[29–31,33,34,36–38] Considering that the lanthanide remains coordinated by 7 oxygen atoms and 2 nitrogen atoms, it is reasonable that a similar conformation would be adopted by the solid. However, there does appear to be a trend towards shorter distances in the XRD structures, especially for the water oxygen and EDTA nitrogen atoms. These atoms are more loosely bound than the EDTA oxygen, which may allow them to exist further from the lanthanide in solution, as compared to the solid samples. In the solid phase of the XRD samples, lack of solvent after crystallization may favor a closer association of these atoms to the lanthanide within the crystal

lattice.[40] A similar phenomenon can be observed when comparing structural XRD and EXAFS data for actinides complexed by polyaminocarboxylates.[23]

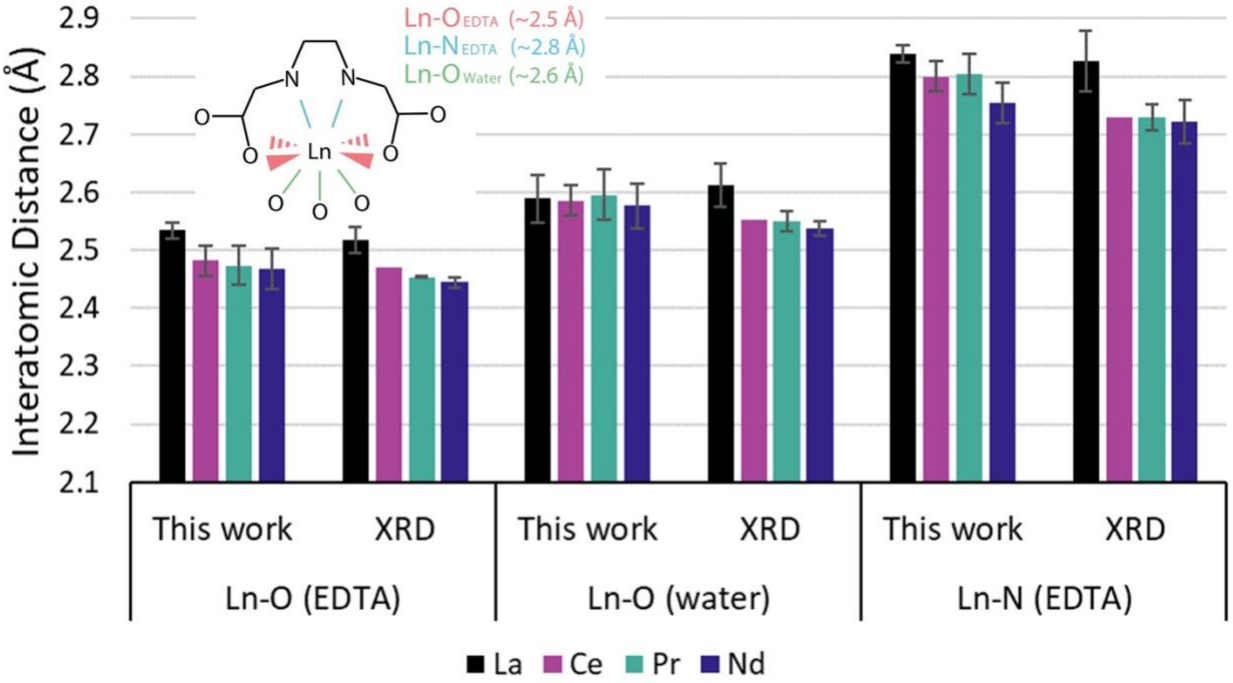

Figure 4: The average distances from the lanthanide atom to coordinating atoms as determined by the best fit EXAFS results of this study and by single crystal XRD from literature.[29–31,33,34,36–38]

There are few studies that have used EXAFS or molecular simulations (MD/DFT) to determine the aqueous-phase structure of the lanthanides with EDTA. EXAFS studies have reported the average distance of coordinated EDTA atoms to the lanthanide in La-EDTA and Nd-EDTA to be 2.48 Å and 2.48 ± 0.09 Å, respectively.[28,41] These distances are considerably shorter than the distances determined in this study (La = 2.62 ± 0.02 Å and Nd = 2.57 ± 0.04 Å). Yamaguchi et al. acknowledged that their distances were short and attributed it to their need to use a one-shell model during EXAFS analysis.[41] The other study is a cited unpublished work that cannot be examined in depth.[28] A molecular dynamics study determined an average La-EDTA distance of 2.53 ± 0.06 Å.[28] All coordinating atoms were consistently ~0.1 Å closer to the Ln than coordinating atoms in

this study, which could be due to the classical (i.e., not quantum) force field employed in the simulations, or due to thermal disorder. An ab-initio molecular dynamics (AIMD) study showed similar EDTA oxygen and EDTA nitrogen distances (2.53 and 2.83 Å, respectively)[39] to distances determined here (2.53 and 2.83 Å, respectively). These results suggest that the bond distances depend on the methods that are used to compute the energy.

Conclusion

The structures of Ln-EDTA coordination complexes (for La, Ce, Pr, and Nd) in aqueous solution were determined using a combined DFT and EXAFS approach. EXAFS fits were of high quality (R-factor < 0.02) and showed similar trends in coordinating atom distances to the DFT structures, indicating that DFT reasonably modeled the Ln-EDTA complexes observed in solution. All four complexes were determined to be 9-coordinate with 6 sites occupied by the EDTA molecule (2 nitrogen atoms and 4 carboxyl oxygen atoms) and 3 sites occupied by oxygen atoms from inner sphere water molecules. The distances of these first shell bonds were slightly longer (~0.03 Å on average) than distances reported in solid-phase XRD studies. This difference in first shell distances emphasizes the need for solution-phase structural characterization in addition to solid-phase XRD structures, when designing liquid separations. Solution-phase literature using EXAFS, MD, and DFT individually showed a range of average coordinating atoms distances to the lanthanide atom (~2.45-2.65 Å).

By combining experimental EXAFS data with DFT optimized reference structures, we have been able to observe the solution phase structure of Ln-EDTA complexes without relying on solid-phase experimental data. Ultimately, DFT calculations, based on structures derived from this combined EXAFS/DFT approach can be used to determine the thermodynamics of complexation for a variety of tunable ligands. These thermodynamic values can then be compared to

experimentally-determined bulk thermodynamic measurements (e.g., from isothermal titration calorimetry[74,75]) to guide the design of REE-selective ligands. Thus, determination of the Ln-EDTA solution-phase structures in this study is the first step towards the design of ligands for sustainable, aqueous REE separations.

Associated Content

Supporting Information Available:

Additional DFT information is provided including input files for geometry optimization, brief discussions of modelling decisions and their impact on the EXAFS model, and binding energy calculations for Ln-EDTA complexes. Also, many additional EXAFS modelling details are provided: input files for FEFF calculations are included, EXAFS spectra before and after MEE removal are compared, the fits for the Ln-EDTA complexes in k-space are available, and a brief discussion of the advantages of the two-shell model is included.

This information is available free of charge at the website: https://urldefense.com/v3/__http://pubs.acs.org/__;!!PTd7Sdtyuw!T2dzlLN0XwHwp7yKsb1w1Y-tEaMt0BEWLQ1hzsoavjrNYUVUtAv1ve7wecPxdq_uEb6nZE7KeMslQ-P1y1yi2PbbkE0-tg$

Notes

The authors declare no competing financial interest.

Acknowledgements

We thank the National Science Foundation for their support (awards 2133530 and 2133512). Also, we thank Lars Ostervold and Ruhi Sultana for their help collecting the EXAFS data. DFT simulations were performed on Clemson University's Palmetto Supercomputing Cluster. Co-ACCESS, is supported by the U.S. Department of Energy, Office of Basic Energy Sciences, Chemical Sciences, Geosciences and Biosciences Division. Use of the Stanford Synchrotron

Radiation Lightsource, SLAC National Accelerator Laboratory, is supported by the U.S. Department of Energy, Office of Science, Office of Basic Energy Sciences under Contract No. DE-AC02-76SF00515. The DMDW simulations used resources of the National Energy Research Scientific Computing Center (NERSC), a U.S. Department of Energy Office of Science User Facility located at Lawrence Berkeley National Laboratory, operated under contract no. DE-AC02-05CH11231 using NERSC award ERCAP0023078.

References

(1) IPCC; Masson-Delmotte, V.; Zhai, P.; Pörtner, H.-O.; Roberts, D.; Skea, J.; Shukla, P.; Pirani, A.; Moufouma-Okia, W.; Péan, C.; Pidcock, R.; Connors, S.; Matthews, R.; Chen, Y.; Zhou, X.; Gomis, M.; Lonnoy, E.; Maycock, T.; Tignor, M.; Tabatabaei, M. *Global Warming of 1.5°C. An IPCC Special Report on the Impacts of Global Warming of 1.5°C above Pre-Industrial Levels and Related Global Greenhouse Gas Emission Pathways, in the Context of Strengthening the Global Response to the Threat of Climate Change, Sustainable Development, and Efforts to Eradicate Poverty*; 2018. https://doi.org/10.1017/9781009157940.

(2) Zhou, B.; Li, Z.; Chen, C. Global Potential of Rare Earth Resources and Rare Earth Demand from Clean Technologies. *Minerals* **2017**, *7* (11), 203. https://doi.org/10.3390/min7110203.

(3) Schreiber, A.; Marx, J.; Zapp, P.; Hake, J.-F.; Voßenkaul, D.; Friedrich, B. Environmental Impacts of Rare Earth Mining and Separation Based on Eudialyte: A New European Way. *Resources* **2016**, *5* (4), 32. https://doi.org/10.3390/resources5040032.

(4) Schreiber, A.; Marx, J.; Zapp, P. Life Cycle Assessment Studies of Rare Earths Production - Findings from a Systematic Review. *Science of The Total Environment* **2021**, *791*, 148257. https://doi.org/10.1016/j.scitotenv.2021.148257.

(5) Navarro, J.; Zhao, F. Life-Cycle Assessment of the Production of Rare-Earth Elements for Energy Applications: A Review. *Frontiers in Energy Research* **2014**, *2* (45), 1–17. https://doi.org/10.3389/fenrg.2014.00045.

(6) Lee, J. C. K.; Wen, Z. Pathways for Greening the Supply of Rare Earth Elements in China. *Nat Sustain* **2018**, *1* (10), 598–605. https://doi.org/10.1038/s41893-018-0154-5.

(7) Xie, F.; Zhang, T. A.; Dreisinger, D.; Doyle, F. A Critical Review on Solvent Extraction of Rare Earths from Aqueous Solutions. *Minerals Engineering* **2014**, *56*, 10–28. https://doi.org/10.1016/j.mineng.2013.10.021.

(8) Vahidi, E.; Zhao, F. Environmental Life Cycle Assessment on the Separation of Rare Earth Oxides through Solvent Extraction. *Journal of Environmental Management* **2017**, *203*, 255–263. https://doi.org/10.1016/j.jenvman.2017.07.076.

(9) Kołodyńska, D.; Fila, D.; Gajda, B.; Gęga, J.; Hubicki, Z. Rare Earth Elements—Separation Methods Yesterday and Today. In *Applications of Ion Exchange Materials in the Environment*; Inamuddin, Ahamed, M. I., Asiri, A. M., Eds.; Springer International Publishing: Cham, 2019; pp 161–185. https://doi.org/10.1007/978-3-030-10430-6_8.

(10) Opare, E. O.; Struhs, E.; Mirkouei, A. A Comparative State-of-Technology Review and Future Directions for Rare Earth Element Separation. *Renewable and Sustainable Energy Reviews* **2021**, *143*, 110917. https://doi.org/10.1016/j.rser.2021.110917.
(11) Gupta, C. K.; Krishnamurthy, N. Extractive Metallurgy of Rare Earths. *International Materials Reviews* **1992**, *37* (1), 197–248. https://doi.org/10.1179/imr.1992.37.1.197.
(12) Fu, F.; Wang, Q. Removal of Heavy Metal Ions from Wastewaters: A Review. *Journal of Environmental Management* **2011**, *92* (3), 407–418. https://doi.org/10.1016/j.jenvman.2010.11.011.
(13) Pereao, O.; Bode-Aluko, C.; Fatoba, O.; Petrik, L.; Laatikainen, K. Rare Earth Elements Removal Techniques from Water/Wastewater: A Review. *Desalination and water treatment* **2018**, *130*, 71–86. https://doi.org/10.5004/dwt.2018.22844.
(14) Hu, Y.; Florek, J.; Larivière, D.; Fontaine, F.-G.; Kleitz, F. Recent Advances in the Separation of Rare Earth Elements Using Mesoporous Hybrid Materials. *The Chemical Record* **2018**, *18* (7–8), 1261–1276. https://doi.org/10.1002/tcr.201800012.
(15) Ellis, R. J.; Brigham, D. M.; Delmau, L.; Ivanov, A. S.; Williams, N. J.; Vo, M. N.; Reinhart, B.; Moyer, B. A.; Bryantsev, V. S. "Straining" to Separate the Rare Earths: How the Lanthanide Contraction Impacts Chelation by Diglycolamide Ligands. *Inorg. Chem.* **2017**, *56* (3), 1152–1160. https://doi.org/10.1021/acs.inorgchem.6b02156.
(16) Brigham, D. M.; Ivanov, A. S.; Moyer, B. A.; Delmau, L. H.; Bryantsev, V. S.; Ellis, R. J. Trefoil-Shaped Outer-Sphere Ion Clusters Mediate Lanthanide(III) Ion Transport with Diglycolamide Ligands. *J. Am. Chem. Soc.* **2017**, *139* (48), 17350–17358. https://doi.org/10.1021/jacs.7b07318.
(17) Stamberga, D.; Healy, M. R.; Bryantsev, V. S.; Albisser, C.; Karslyan, Y.; Reinhart, B.; Paulenova, A.; Foster, M.; Popovs, I.; Lyon, K.; Moyer, B. A.; Jansone-Popova, S. Structure Activity Relationship Approach toward the Improved Separation of Rare-Earth Elements Using Diglycolamides. *Inorg. Chem.* **2020**, *59* (23), 17620–17630. https://doi.org/10.1021/acs.inorgchem.0c02861.
(18) Batchu, N. K.; Li, Z.; Verbelen, B.; Binnemans, K. Structural Effects of Neutral Organophosphorus Extractants on Solvent Extraction of Rare-Earth Elements from Aqueous and Non-Aqueous Nitrate Solutions. *Separation and Purification Technology* **2021**, *255*, 117711. https://doi.org/10.1016/j.seppur.2020.117711.
(19) Nash, K. L. Aqueous Complexes in Separations of F-Elements: Options and Strategies for Future Development. *Separation Science and Technology* **1999**, *34* (6–7), 911–929. https://doi.org/10.1080/01496399908951073.
(20) Higgins, R. F.; Ruoff, K. P.; Kumar, A.; Schelter, E. J. Coordination Chemistry-Driven Approaches to Rare Earth Element Separations. *Acc. Chem. Res.* **2022**, *55* (18), 2616–2627. https://doi.org/10.1021/acs.accounts.2c00312.
(21) Nash, K. L.; Choppin, G. R. Separations Chemistry for Actinide Elements: Recent Developments and Historical Perspective. *Separation Science and Technology* **1997**, *32* (1–4), 255–274. https://doi.org/10.1080/01496399708003198.
(22) Audras, M.; Berthon, L.; Berthon, C.; Guillaumont, D.; Dumas, T.; Illy, M.-C.; Martin, N.; Zilbermann, I.; Moiseev, Y.; Ben-Eliyahu, Y.; Bettelheim, A.; Cammelli, S.; Hennig, C.; Moisy, P. Structural Characterization of Am(III)- and Pu(III)-DOTA Complexes. *Inorg. Chem.* **2017**, *56* (20), 12248–12259. https://doi.org/10.1021/acs.inorgchem.7b01666.
(23) Bonin, L.; Guillaumont, D.; Jeanson, A.; Den Auwer, C.; Grigoriev, M.; Berthet, J.-C.; Hennig, C.; Scheinost, A.; Moisy, Ph. Thermodynamics and Structure of Actinide(IV)

Complexes with Nitrilotriacetic Acid. *Inorg. Chem.* **2009**, *48* (9), 3943–3953. https://doi.org/10.1021/ic801453w.
(24) Lahrouch, F.; Siberchicot, B.; Fèvre, J.; Leost, L.; Aupiais, J.; Solari, P. L.; Den Auwer, C.; Di Giorgio, C. Carboxylate- and Phosphonate-Modified Polyethylenimine: Toward the Design of Actinide Decorporation Agents. *Inorg. Chem.* **2020**, *59* (1), 128–137. https://doi.org/10.1021/acs.inorgchem.9b02014.
(25) Zhang, K.; Dai, Z.; Zhang, W.; Gao, Q.; Dai, Y.; Xia, F.; Zhang, X. EDTA-Based Adsorbents for the Removal of Metal Ions in Wastewater. *Coordination Chemistry Reviews* **2021**, *434*, 213809. https://doi.org/10.1016/j.ccr.2021.213809.
(26) Kronholm, B.; Anderson, C. G.; Taylor, P. R. A Primer on Hydrometallurgical Rare Earth Separations. *JOM* **2013**, *65* (10), 1321–1326. https://doi.org/10.1007/s11837-013-0718-9.
(27) Chen, B.; He, M.; Zhang, H.; Jiang, Z.; Hu, B. Chromatographic Techniques for Rare Earth Elements Analysis. *Physical Sciences Reviews* **2017**, *2* (4), 20160057. https://doi.org/10.1515/psr-2016-0057.
(28) Durand, S.; Dognon, J.-P.; Guilbaud, P.; Rabbe, C.; Wipff, G. Lanthanide and Alkaline-Earth Complexes of EDTA in Water : A Molecular Dynamics Study of Structures and Binding Selectivities. *Journal of the Chemical Society, Perkin Transactions 2* **2000**, *0* (4), 705–714. https://doi.org/10.1039/A908879B.
(29) Matković-Čalogović, D. Structure of Potassium Triaqua(Ethylenediaminetetraacetato)Neodymate(III) Pentahydrate. *Acta Cryst C* **1988**, *44* (3), 435–437. https://doi.org/10.1107/S0108270187011004.
(30) Nakamura, K.; Kurisaki, T.; Wakita, H.; Yamaguchi, T. Sodium Triaqua(Ethylenediaminetetraacetato)Lanthanate(III) Pentahydrate and the Isomorphous Neodymium(III) and Europium(III) Salts. *Acta Cryst C* **1995**, *51* (8), 1559–1563. https://doi.org/10.1107/S0108270195001843.
(31) Ragul, R.; Sivasankar, B. N. Syntheses, Characterization and Structural Determination of Nine Coordinated N2H5[Ce(Edta)(H2O)3]·4H2O and N2H5[Eu(Edta)(H2O)3]·4H2O. *J Chem Crystallogr* **2011**, *41* (9), 1273–1279. https://doi.org/10.1007/s10870-011-0087-6.
(32) Sakagami, N.; Yamada, Y.; Konno, T.; Okamoto, K. Crystal Structures and Stereochemical Properties of Lanthanide(III) Complexes with Ethylenediamine-N,N,N′,N′-Tetraacetate. *Inorganica Chimica Acta* **1999**, *288* (1), 7–16. https://doi.org/10.1016/S0020-1693(99)00005-5.
(33) Ragul, R.; Sivasankar, B. N. Synthesis, Structure, Antioxidant, and Antiviral Studies on N2H5[Ln(Edta)(H2O)3].5H2O (Ln = Pr, Nd, and Sm). *Synthesis and Reactivity in Inorganic, Metal-Organic, and Nano-Metal Chemistry* **2013**, *43* (4), 382–389. https://doi.org/10.1080/15533174.2012.740736.
(34) Mullins, J. M. Structures of Lanthanide-Edta Complexes. Master Thesis, University of Cape Town, 1983. https://open.uct.ac.za/handle/11427/22209 (accessed 2023-02-08).
(35) Mathur, J. N.; Thakur, P.; Dodge, C. J.; Francis, A. J.; Choppin, G. R. Coordination Modes in the Formation of the Ternary Am(III), Cm(III), and Eu(III) Complexes with EDTA and NTA: TRLFS, 13C NMR, EXAFS, and Thermodynamics of the Complexation. *Inorg. Chem.* **2006**, *45* (20), 8026–8035. https://doi.org/10.1021/ic052166c.
(36) Hoard, J. L.; Lee, B.; Lind, M. D. On the Structure-Dependent Behavior of Ethylenediaminetetraacetato Complexes of the Rare Earth Ln3+ Ions1. *J. Am. Chem. Soc.* **1965**, *87* (7), 1612–1613. https://doi.org/10.1021/ja01085a037.

(37) Xiong, D.-B.; Chen, H.-H.; Yang, X.-X.; Zhao, J.-T. Hydrothermal Synthesis and Characterization of a New 1-D Polymeric Lanthanum Ethylenediaminetetraacetate with Less Metal-Aqua Coordination: {[La(EDTA)(H2O)]2}n. *Inorganica Chimica Acta* **2007**, *360* (5), 1616–1620. https://doi.org/10.1016/j.ica.2006.08.044.
(38) Huang, X.-H.; Xu, X.-H.; Pan, W.-B.; Zeng, R.-H. Poly[Aqua-[μ-N′-(Carboxymethyl)Ethylene-diamine--N,N,N′-Triacetato]Neodymium(III)]. *Acta Cryst E* **2008**, *64* (9), m1194–m1194. https://doi.org/10.1107/S1600536808026445.
(39) D. O'Brien, R.; J. Summers, T.; S. Kaliakin, D.; C. Cantu, D. The Solution Structures and Relative Stability Constants of Lanthanide–EDTA Complexes Predicted from Computation. *Physical Chemistry Chemical Physics* **2022**, *24* (17), 10263–10271. https://doi.org/10.1039/D2CP01081J.
(40) Levina, A.; Armstrong, R. S.; Lay, P. A. Three-Dimensional Structure Determination Using Multiple-Scattering Analysis of XAFS: Applications to Metalloproteins and Coordination Chemistry. *Coordination Chemistry Reviews* **2005**, *249* (1), 141–160. https://doi.org/10.1016/j.ccr.2004.10.008.
(41) Yamaguchi, T.; Nakamura, K.; Wakita, H.; Nomura, M. An Extended X-Ray Absorption Fine Structure Study of Lanthanide(III) Aqua and Polyaminopolycarboxylate Complexes in Aqueous Solution. In *Proceedings of the Workshop on Actinides Solution Chemistry*; World Scientific Publishing Co. Pte. Ltd, 1997; pp 165–180. https://doi.org/10.1142/9789814530965.
(42) Chen, Y.; Rana, R.; Sours, T.; Vila, F. D.; Cao, S.; Blum, T.; Hong, J.; Hoffman, A. S.; Fang, C.-Y.; Huang, Z.; Shang, C.; Wang, C.; Zeng, J.; Chi, M.; Kronawitter, C. X.; Bare, S. R.; Gates, B. C.; Kulkarni, A. R. A Theory-Guided X-Ray Absorption Spectroscopy Approach for Identifying Active Sites in Atomically Dispersed Transition-Metal Catalysts. *J. Am. Chem. Soc.* **2021**, *143* (48), 20144–20156. https://doi.org/10.1021/jacs.1c07116.
(43) Migliorati, V.; Serva, A.; Sessa, F.; Lapi, A.; D'Angelo, P. Influence of Counterions on the Hydration Structure of Lanthanide Ions in Dilute Aqueous Solutions. *J. Phys. Chem. B* **2018**, *122* (10), 2779–2791. https://doi.org/10.1021/acs.jpcb.7b12571.
(44) Shiery, R. C.; Fulton, J. L.; Balasubramanian, M.; Nguyen, M.-T.; Lu, J.-B.; Li, J.; Rousseau, R.; Glezakou, V.-A.; Cantu, D. C. Coordination Sphere of Lanthanide Aqua Ions Resolved with Ab Initio Molecular Dynamics and X-Ray Absorption Spectroscopy. *Inorg. Chem.* **2021**, *60* (5), 3117–3130. https://doi.org/10.1021/acs.inorgchem.0c03438.
(45) D'Angelo, P.; Migliorati, V.; Gibiino, A.; Busato, M. Direct Observation of Contact Ion-Pair Formation in La3+ Methanol Solution. *Inorg. Chem.* **2022**, *61* (43), 17313–17321. https://doi.org/10.1021/acs.inorgchem.2c02932.
(46) Migliorati, V.; Gibiino, A.; Lapi, A.; Busato, M.; D'Angelo, P. On the Coordination Chemistry of the Lanthanum(III) Nitrate Salt in EAN/MeOH Mixtures. *Inorg. Chem.* **2021**, *60* (14), 10674–10685. https://doi.org/10.1021/acs.inorgchem.1c01375.
(47) Grimmel, S.; Schoendorff, G.; Wilson, A. K. Gauging the Performance of Density Functionals for Lanthanide-Containing Molecules. *J. Chem. Theory Comput.* **2016**, *12* (3), 1259–1266. https://doi.org/10.1021/acs.jctc.5b01193.
(48) Weigend, F.; Ahlrichs, R. Balanced Basis Sets of Split Valence, Triple Zeta Valence and Quadruple Zeta Valence Quality for H to Rn: Design and Assessment of Accuracy. *Physical Chemistry Chemical Physics* **2005**, *7* (18), 3297–3305. https://doi.org/10.1039/B508541A.
(49) Pantazis, D. A.; Neese, F. All-Electron Scalar Relativistic Basis Sets for the Lanthanides. *J. Chem. Theory Comput.* **2009**, *5* (9), 2229–2238. https://doi.org/10.1021/ct900090f.

(50) Dolg, M.; Stoll, H.; Preuss, H. A Combination of Quasirelativistic Pseudopotential and Ligand Field Calculations for Lanthanoid Compounds. *Theoret. Chim. Acta* **1993**, *85* (6), 441–450. https://doi.org/10.1007/BF01112983.
(51) Dolg, M.; Stoll, H.; Savin, A.; Preuss, H. Energy-Adjusted Pseudopotentials for the Rare Earth Elements. *Theoret. Chim. Acta* **1989**, *75* (3), 173–194. https://doi.org/10.1007/BF00528565.
(52) Yappert, M. C.; DuPre, D. B. Complexometric Titrations: Competition of Complexing Agents in the Determination of Water Hardness with EDTA. *J. Chem. Educ.* **1997**, *74* (12), 1422. https://doi.org/10.1021/ed074p1422.
(53) Zaitoun, M. A.; Lin, C. T. Chelating Behavior between Metal Ions and EDTA in Sol−Gel Matrix. *J. Phys. Chem. B* **1997**, *101* (10), 1857–1860. https://doi.org/10.1021/jp963102d.
(54) Vila, F. D.; Rehr, J. J.; Rossner, H. H.; Krappe, H. J. Theoretical X-Ray Absorption Debye-Waller Factors. *Phys. Rev. B* **2007**, *76* (1), 014301. https://doi.org/10.1103/PhysRevB.76.014301.
(55) Ravel, B.; Newville, M. ATHENA, ARTEMIS, HEPHAESTUS: Data Analysis for X-Ray Absorption Spectroscopy Using IFEFFIT. *J Synchrotron Rad* **2005**, *12* (4), 537–541. https://doi.org/10.1107/S0909049505012719.
(56) Henke, B. L.; Gullikson, E. M.; Davis, J. C. X-Ray Interactions: Photoabsorption, Scattering, Transmission, and Reflection at E = 50-30,000 EV, Z = 1-92. *Atomic Data and Nuclear Data Tables* **1993**, *54* (2), 181–342. https://doi.org/10.1006/adnd.1993.1013.
(57) Solera, J. A.; García, J.; Proietti, M. G. Multielectron Excitations at the *L* Edges in Rare-Earth Ionic Aqueous Solutions. *Phys. Rev. B* **1995**, *51* (5), 2678–2686. https://doi.org/10.1103/PhysRevB.51.2678.
(58) Ohta, A.; Kagi, H.; Nomura, M.; Tsuno, H.; Kawabe, I. Coordination Study of Rare Earth Elements on Fe Oxyhydroxide and Mn Dioxides: Part I. Influence of a Multi-Electron Excitation on EXAFS Analyses of La, Pr, Nd, and Sm. *American Mineralogist* **2009**, *94* (4), 467–475. https://doi.org/10.2138/am.2009.2986.
(59) Chaboy, J.; Marcelli, A.; Tyson, T. A. Influence of Double-Electron Transitions on the EXAFS L Edges of Rare-Earth Systems. *Phys. Rev. B* **1994**, *49* (17), 11652–11661. https://doi.org/10.1103/PhysRevB.49.11652.
(60) Ohta, A.; Kagi, H.; Tsuno, H.; Nomura, M.; Kawabe, I. Influence of Multi-Electron Excitation on EXAFS Spectroscopy of Trivalent Rare-Earth Ions and Elucidation of Change in Hydration Number through the Series. *American Mineralogist* **2008**, *93* (8–9), 1384–1392. https://doi.org/10.2138/am.2008.2628.
(61) Calvin, S. *XAFS for Everyone*; CRC Press: Boca Raton, 2013. https://doi.org/10.1201/b14843.
(62) D'Angelo, P.; Zitolo, A.; Migliorati, V.; Persson, I. Analysis of the Detailed Configuration of Hydrated Lanthanoid(III) Ions in Aqueous Solution and Crystalline Salts by Using K- and L3-Edge XANES Spectroscopy. *Chemistry – A European Journal* **2010**, *16* (2), 684–692. https://doi.org/10.1002/chem.200900122.
(63) Ravel, B. Path Degeneracy and EXAFS Analysis of Disordered Materials. *J Synchrotron Rad* **2014**, *21* (6), 1269–1274. https://doi.org/10.1107/S1600577514014982.
(64) Allen, P. G.; Bucher, J. J.; Shuh, D. K.; Edelstein, N. M.; Craig, I. Coordination Chemistry of Trivalent Lanthanide and Actinide Ions in Dilute and Concentrated Chloride Solutions. *Inorg. Chem.* **2000**, *39* (3), 595–601. https://doi.org/10.1021/ic9905953.

(65) Moreau, J.; Guillon, E.; Pierrard, J.-C.; Rimbault, J.; Port, M.; Aplincourt, M. Complexing Mechanism of the Lanthanide Cations Eu3+, Gd3+, and Tb3+ with 1,4,7,10-Tetrakis(Carboxymethyl)-1,4,7,10-Tetraazacyclododecane (Dota)—Characterization of Three Successive Complexing Phases: Study of the Thermodynamic and Structural Properties of the Complexes by Potentiometry, Luminescence Spectroscopy, and EXAFS. *Chemistry – A European Journal* **2004**, *10* (20), 5218–5232. https://doi.org/10.1002/chem.200400006.

(66) Alex Brown, M.; Brossard, T.; Rotsch, D. A. Examination of Lutetium(III)-DOTA and Copper(II)-NOTA Solution Structures Using EXAFS. *Inorganica Chimica Acta* **2018**, *482*, 118–121. https://doi.org/10.1016/j.ica.2018.05.031.

(67) Moreau, G.; Burai, L.; Helm, L.; Purans, J.; Merbach, A. E. Structural XAFS Investigation of Eu2+ and Sr2+ Poly(Amino Carboxylates): Consequences for Water Exchange Rates on MRI-Relevant Complexes. *J. Phys. Chem. A* **2003**, *107* (5), 758–769. https://doi.org/10.1021/jp0267510.

(68) Thakur, P.; Conca, J. L.; Dodge, C. J.; Francis, A. J.; Choppin, G. R. Complexation Thermodynamics and Structural Studies of Trivalent Actinide and Lanthanide Complexes with DTPA, MS-325 and HMDTPA. *Radiochimica Acta* **2013**, *101* (4), 221–232. https://doi.org/10.1524/ract.2013.2018.

(69) Moreau, J.; Guillon, E.; Aplincourt, P.; Pierrard, J.-C.; Rimbault, J.; Port, M.; Aplincourt, M. Thermodynamic and Structural Properties of Eu3+, Gd3+ and Tb3+ Complexes with 1,4,7,10-Tetra(2-Glutaryl)-1,4,7,10-Tetraazacyclododecane in Solution: EXAFS, Luminescence, Potentiometric Studies, and Quantum Calculations. *European Journal of Inorganic Chemistry* **2003**, *2003* (16), 3007–3020. https://doi.org/10.1002/ejic.200300085.

(70) Driscoll, D. M.; Shiery, R. C.; Balasubramanian, M.; Fulton, J. L.; Cantu, D. C. Ionic Contraction across the Lanthanide Series Decreases the Temperature-Induced Disorder of the Water Coordination Sphere. *Inorg. Chem.* **2022**, *61* (1), 287–294. https://doi.org/10.1021/acs.inorgchem.1c02837.

(71) Parker, D.; Dickins, R. S.; Puschmann, H.; Crossland, C.; Howard, J. A. K. Being Excited by Lanthanide Coordination Complexes: Aqua Species, Chirality, Excited-State Chemistry, and Exchange Dynamics. *Chem. Rev.* **2002**, *102* (6), 1977–2010. https://doi.org/10.1021/cr010452+.

(72) Kelley, M. P.; Deblonde, G. J.-P.; Su, J.; Booth, C. H.; Abergel, R. J.; Batista, E. R.; Yang, P. Bond Covalency and Oxidation State of Actinide Ions Complexed with Therapeutic Chelating Agent 3,4,3-LI(1,2-HOPO). *Inorg. Chem.* **2018**, *57* (9), 5352–5363. https://doi.org/10.1021/acs.inorgchem.8b00345.

(73) Jordan, R. B. Lanthanide Contraction: What Is Normal? *Inorg. Chem.* **2023**, *62* (9), 3715–3721. https://doi.org/10.1021/acs.inorgchem.2c03674.

(74) Michels, J. J.; Huskens, J.; Reinhoudt, D. N. Noncovalent Binding of Sensitizers for Lanthanide(III) Luminescence in an EDTA-Bis(β-Cyclodextrin) Ligand. *J. Am. Chem. Soc.* **2002**, *124* (9), 2056–2064. https://doi.org/10.1021/ja017025y.

(75) Hatanaka, T.; Kikkawa, N.; Matsugami, A.; Hosokawa, Y.; Hayashi, F.; Ishida, N. The Origins of Binding Specificity of a Lanthanide Ion Binding Peptide. *Sci Rep* **2020**, *10* (1), 19468. https://doi.org/10.1038/s41598-020-76527-y.

Table of Contents Synopsis

Aqueous phase La-, Ce-, Pr-, and Nd-EDTA coordination structures were determined using extended x-ray absorption fine structure modelling of density functional theory simulated structures and the distances of first shell coordinating atoms were compared to those determined by x-ray diffraction.

Table of Contents Graphic